Structural characterization of nano-sized calcium deficient apatite powders

Sz-Chian Liou[a], San-Yuan Chen[a,*], Hsin-Yi Lee[b], Jong-Shing Bow[c]

[a] *Department of Materials Science and Engineering, National Chiao-Tung University, 1001 Ta-Hsueh Road, Hsinchu 300, Taiwan, ROC*
[b] *National Synchrotron Radiation Research Center, Hsinchu 300, Taiwan, ROC*
[c] *QA12A/FA of United Microelectronics Cooperation, Tainan 744, Taiwan, ROC*

Abstract

Nano-sized calcium-deficient apatitic (CDHA) crystals with Ca/P ratios from 1.5 to 1.67 were synthesized using wet chemical method and of needle-like shape with 5–10 nm in diameter and 40–50 nm in length was observed. The structural environment of the Ca atoms in all the CDHA nano-crystals has been investigated using EXAFS, XANES and EELS. The results reveal that a maximum Fourier transform amplitude occurs at the apatite with a Ca/P ratio of 1.67 and the structural disorder increase following the sequence of $1.67 > 1.5 > 1.6 > 1.55$. A similar phenomenon is also observed in both K-edge XANES and $L_{2,3}$-edge ELNES in the Ca atom. The structural analysis further demonstrates that different chemical and biological properties among these CDHA nano-crystals with Ca/P ratio from 1.5 to 1.67 are primarily due to the effect of stoichiometry and non-stoichiometry as compared to the structural order–disorder.
© 2003 Elsevier Ltd. All rights reserved.

1. Introduction

Bioactive ceramic materials, such as hydroxyapatite [$Ca_{10}(PO_4)_6(OH)_2$, HA] were widely used as bone substitutes for several decades. Among these bioceramics, particular attention has been given to HA due to its bioactivity [1,2]. Stoichiometric hydroxyapatite [$Ca_{10}(PO_4)_6(OH)_2$] has a hexagonal structure constructed from columns of Ca and O atoms which are parallel to the hexagonal axis with lattice constants of $a = 0.9418$ nm and $c = 0.6884$ nm [3]. On the other hand, the calcium-deficient hydroxyapatites [$Ca_{10-x}(PO_4)_{6-x}(HPO_4)_x(OH)_{2-x}$, $0 \leqslant x \leqslant 1$, CDHA] are of greater biological interest than stoichiometric HA since the Ca/P ratio in bone is nearer to 1.5 [1,2]. It has been suggested that calcium-deficient apatitic (CDHA) plays important roles in several processes such as bone remodeling and bone formation. Furthermore,

both compositions are chemically and structurally similar to the mineral constituent of human hard tissue. However, bone mineral (natural biocrystal) essentially has a CDHA structure with a Ca/P ratio of about 1.5 which, strictly speaking, is a Ca/P ratio similar to tricalcium phosphates (TCP), $Ca_3(PO_4)_2$, (Ca/P = 1.5) but structurally and chemically compositionally similar to stoichiometric hydroxyapatite, $Ca_{10}(PO_4)_6(OH)_2$, (Ca/P = 1.67). It was also reported that the chemical properties such as catalysis, ion-exchange and degradation in solution are strongly dependent on Ca/P ratios [4–10]. However, the CDHA with the Ca/P ratios ranging from 1.5 to 1.67 appears indistinguishable from one another in X-ray diffraction (XRD) patterns. Therefore, it is generally difficult to correlate these chemical properties and their changes with Ca/P ratios, even with possible structure changes, by XRD measurement.

Recently, various processes have been developed to prepare nano-sized apatite powders [11–15]. Among these processes, in situ synthesis of CDHA nano-crystals at ambient temperature via a simple coprecipitation process is one of most attractive routes and has not been

---

*Corresponding author. Tel.: +886-3-573-1818; fax: +886-3-5724727.

E-mail address: sychen@cc.nctu.edu.tw (S.-Y. Chen).

reported. Therefore, we first focus on the in situ synthesis of CDHA nano-crystals with different Ca/P ratios ranging from 1.5 to 1.67. The structure characteristics of the synthesized CDHA nano-crystals with different Ca/P ratios will be analyzed by FT-IR, XRD, TEM, X-ray absorption spectroscopy (XAS) and electron energy loss spectroscopy (EELS) to clarify structural differences between these CDHA nano-crystals.

2. Experimental procedure

2.1. Powder synthesis

The analytical grade reagent $(CH_3COO)_2Ca \cdot xH_2O$ (99%, Aldrich Chemical company, Inc., USA) and H_3PO_4 (99%, Riedel-deHaen, Seelze, Germany) were used as the Ca and P sources in this investigation, respectively. The H_3PO_4 aqueous solutions were first dissolved in deionized water and then slowly dropped (5 cm^3/min) into the vigorously stirred (at a rate of 350 rpm) $(CH_3COO)_2Ca \cdot xH_2O$ aqueous solution with molar ratios of Ca/P = 1.5, 1.55, 1.6 and 1.67 for 2 h. Ammonia solution (25%, Merck) was used to keep the solution at pre-determined pH level (close to 10) throughout the entire synthesis procedure, and the reaction was carried out at room temperature. After filtering and washing several times with deionized water, the mixture was dried overnight at 100°C.

2.2. Powder characterization

2.2.1. Phase analysis

Fourier transform Infrared ray (FT-IR) spectra were performed using KBr pellets (2 mg/300 mg KBr) on a spectrometer (Model 580, Perkin-Elmer) with a resolution of 4.00 cm^{-1}. Infrared spectra were recorded in the range of 4000–400 cm^{-1} to evaluate the function group of the specimens. X-ray diffractometer (M18XHF, MAC Science, Tokyo, Japan) was used for determining the crystalline phase of the synthesized powders at a 4° 2θ per min over a range of $2\theta = 20-60°$.

2.2.2. X-ray absorption measurements

X-ray absorption measurements at the K-edge of Ca were performed on Beamline 15B of the National Synchrotron Radiation Research Center (NSRRC) in Taiwan. Si (1 1 1) crystals in a fixed exit double crystal monochromator were used to monochromatize bending magnet radiation from the electron storage ring operating at 1.5 GeV with an average current of 150 mA. The spectra of the bulk materials were measured in the fluorescence mode. The incident beam had a cross-section of 3×20 mm^2 and intersected with the specimen surface at 45°. An ion chamber was used as the

fluorescence detector, positioned such that the detector window centerline also intersected with the specimen surface at 45° but was perpendicular to the incident beam direction. For the bulk samples, the fluorescence intensity $I_F(E)$ was normalized by the incident intensity $I_0(E)$ to obtain the absorption spectrum, $\mu(E) = I_F(E)/I_0(E)$. A linear function was fitted to the pre-edge region of $\mu(E)$ and was subtracted from $\mu(E)$ in order to isolate the contributions from K-shell absorption, $\mu_K(E)$. The EXAFS function, $\chi(k)$, was extracted from $\mu_K(E)$ using standard procedures: a smooth background, $\mu_0(E)$, was subtracted from $\mu_K(E)$, and then the spectra were normalized by the average value of the $\mu_0(E)$ throughout the EXAFS region. Then $k^3\chi(k)$ was Fourier-transformed to obtain the radial distribution function of backscattering atoms around the Ca atom.

2.2.3. Transmission electron microscopy (TEM) analysis

The powdered sample was ultrasonically dispersed in acetone to form very dilute suspensions and then a few droplets were dropped on copper grids with a carbon-coated film. Microstructure observations were performed in a Philips Tecnai 20 (Holland, The Netherlands) microscope operating at 200 keV and equipped with a Gatan image filter (GIF, Model GIF-2000) for EELS analysis. EELS spectra were obtained with an energy resolution of 1 eV (zero-loss peak) and an energy dispersion of 0.2 eV per channel. The EELS was capable of analyzing Ca, but not P. The background below the edges was determined by fitting the inverse power-law AE^{-r}, where E is the energy loss and A and r are constants to the spectrum before the ionization threshold and extrapolating this function over a certain energy range.

3. Results and discussion

3.1. Phase identification

Molecular arrangement of the precipitate powders can be further identified through the use of FT-IR analysis, where as selectively shown in Fig. 1 are the IR spectra of the powders prepared in the presence of Ca/P ratios from 1.5 to 1.67. The bands at 1092 and 1040 cm^{-1} are assigned to the components of the triply degenerate ν_3 antisymmetric P–O stretching mode. The 962 cm^{-1} band is assigned to ν_1, the non-degenerate P–O symmetric stretching mode. The bands at 601 and 571 cm^{-1} are assigned to components of the triply degenerate ν_4 O–P–O bending mode and the bands in the range of 462–474 cm^{-1} are assigned to the components of the doubly degenerate ν_2 O–P–O bending mode. A very weak band near 875 cm^{-1} is the P–O(H) stretching in HPO_4^{2-} groups. Molecular and adsorbed water bands are also discerned at 1640 and 3400 cm^{-1}. A
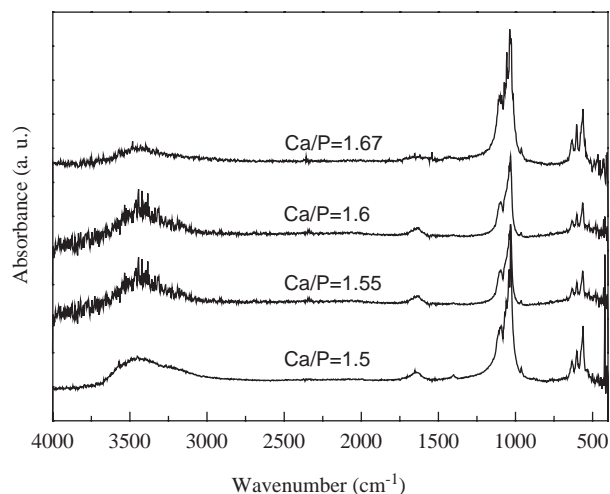
Fig. 1. FT-IR spectra of the precipitated calcium-deficient apatite powders with Ca/P ratios of 1.5, 1.55, 1.6 and 1.67.
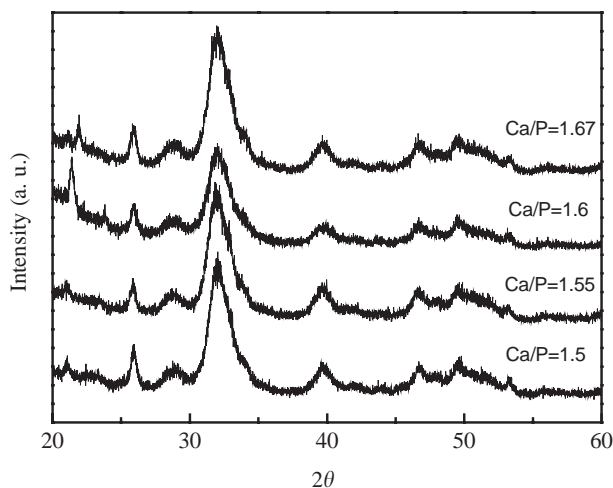

Fig. 2. XRD patterns of the precipitated calcium-deficient apatite powders with Ca/P ratios of 1.5, 1.55, 1.6 and 1.67.

significant concentration of hydroxyl groups remains in the structure as observed from the intensity of the stretching and librational bands at 3572 and $632\,cm^{-1}$ [16]. These IR spectra further confirm that the apatitic structure of the nano-crystals is chemically and structurally identified to be CDHA.

The XRD patterns of the CDHA with Ca/P ratios of 1.5, 1.55, 1.6 and 1.67 are shown in Fig. 2. It was observed that they are essentially indistinguishable from each other. Two major characteristic diffraction peaks can be obtained for all the powdered samples: one near 2θ of $\sim 26°$ and the other broad one at $\sim 32°$. These peaks are almost identical to those of stoichiometric microcrystalline HA (sm-HA), but present much poorer diffraction resolution compared to sm-HA, particularly at $2\theta \sim 32°$. This suggests that the synthetic powders are apatite-like crystals and considered to be a CDHA according to ICDD No. 9-432. This further reflects that

it is difficult to discern the differences between CDHA powders with different Ca/P ratios from 1.5 to 1.67.

3.2. Powder morphology and nano-structure analysis

Fig. 3 shows the TEM bright-field (BF) image of the precipitated CDHA powders with different Ca/P ratios from 1.5 to 1.67. The powder morphology presents a needle-like shape and the needle-like particles are easily developed to form aggregates when higher concentration and fast mixing are applied during the solution preparation [16–18]. The dimension of these CDHA crystals in both radial (diameter) and axial (length) directions is 5–10 nm in diameter and 40–50 nm in length in terms of different Ca/P ratios. An axial zone in some needle-like CDHA particles can be clearly observed in the high-resolution TEM of Fig. 4. The lattice fringes were seen predominantly in long needle-like crystallites and parallel to (1 0 0) CDHA with a width of 0.82 nm. It was suggested that the HA crystals tend to grow along the [0 0 0 1] direction and the fastest growth direction results in needle-like morphology [16]. Under TEM analysis, it was found that the nano-size CDHA crystal is susceptible to electronic beam bombardment that is likely due to the conversion of hydrogen ions into hydrogen gas and may lead to such a transformation or shape change [16–17,19–20].

3.3. X-ray absorption analysis

In an attempt to interpret the difference between CDHA nano-crystals with different Ca/P ratios, the crystallographic viewpoint can be considered. If any defects such as calcium vacancies exist in the structure of CDHA and the same structure is maintained, the bond length and bond angle should be rearranged within localization positions. XAS can be employed to correlate fine structure changes with variations in the Ca/P ratios of calcium-deficient apatites because XAS, including extended X-ray absorption fine structure (EXAFS) and X-ray absorption near-edge structure (XANES) is an element-specific local probe which is sensitive to local structure change [21].

Fourier transforms (FT) of the k^3-weighted Ca K-edge EXAFS oscillation for CDHA nano-crystals with different Ca/P ratios from 1.5 to 1.67 are shown in Fig. 5(a), respectively. The peak height of the FT is related to the backscattering of the photoelectrons by the coordinated and damped atoms due to disorder in the scattering shell. These spectra are almost indistinguishable from each other, suggesting that they all correspond to the same characteristic spectrum of the stoichiometric HA. The main difference between the spectra is the amplitude at the first peak around 0.25 nm and magnified and illustrated in Fig. 5(b). It was known that the first peak of the FT spectrum in the HA crystal
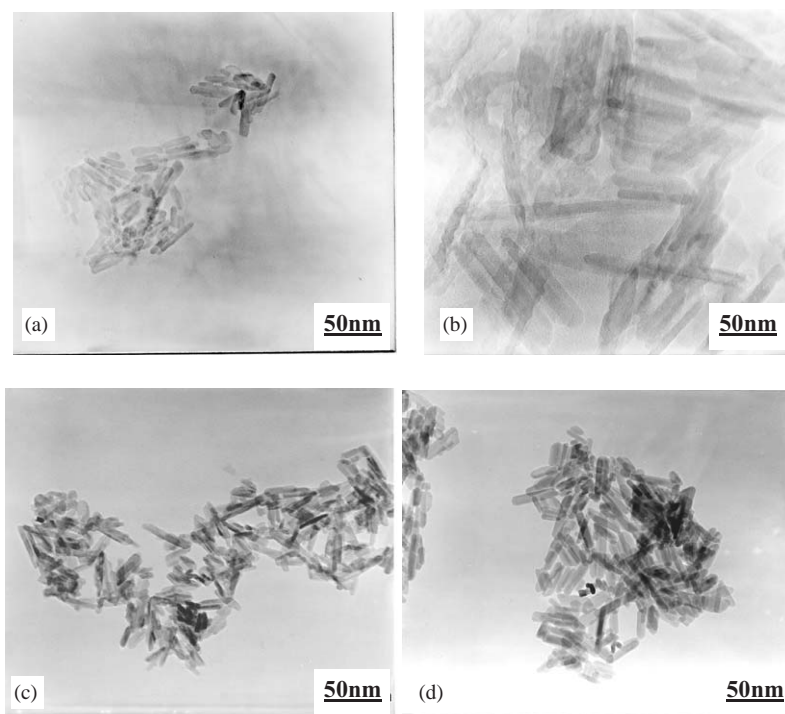
Fig. 3. TEM micrographs of calcium-deficient apatites with different Ca/P ratios: (a) Ca/P = 1.5, (b) Ca/P = 1.55, (c) Ca/P = 1.6 and (d) Ca/P = 1.67.

corresponds to the first coordination sphere of six oxygen atoms [22]. The variation in the FT amplitude seems to indicate that the local structure change exists in the first coordination shell with different Ca/P ratios. According to the chemical formula of CDHA $[Ca_{10-x}(HPO_4)_x(PO_4)_{6-x}(OH)_{2-x}]$, the calcium vacancies probably form localized short-range disorder in the CDHA structure and therefore decrease the amplitude in the FT spectrum. The degree of disorder increases with the decrease of the Ca/P ratio from 1.67 to 1.5, but the FT amplitude shown in Fig. 5 follows $1.67 > 1.5 > 1.6 > 1.55$. It seems to imply that the concept of structural disorder cannot fully elucidate the difference of FT amplitude. One possible explanation is proposed to interpret the difference of FT amplitude in the CDHA with different Ca/P ratios by combining the concept of structure disorder with stoichiometry and non-stoichiometry.

Based on the crystal chemistry, a non-stoichiometric compound is defined to have the chemical formula without a simple integer ratio of atoms and usually exhibits a range of composition [23,24]. Following this viewpoint, all the CDHA crystals in our study can be categorized into two types: one type is stoichiometric HA, Ca/P value of 1.67, and the other is non-stoichiometric apatites with Ca/P ratios of 1.5, 1.55, and 1.6. It should be pointed out that the apatite with the Ca/P ratio of 1.5 is a special non-stoichiometric apatite that was called apatite-tricalcium phosphate (apatite-TCP) [25]. The apatite-TCP $[Ca_9(PO_4)_6(OH)]$

possesses the same Ca/P ratio (1.5) as TCP $[Ca_3(PO_4)_2]$, but both have different a crystal structure and chemical formula. The crystal structure of the apatite-TCP is identified as similar to HA (apatite crystal structure) but different from that of TCP (i.e., β-TCP is a rhombohedral structure). Therefore, the FT amplitude of stoichiometric HA and apatite-TCP is higher than that of non-stoichiometric apatites. This result seems to indicate that the structure disorder plays an important role in the FT amplitude.

Fig. 6(a) further illustrates the Ca K-edge XANES spectra of CDHA with Ca/P ratios of 1.5, 1.55, 1.6 and 1.67. The shape of the XANES spectra and the edge position of all the CDHA crystals are similar, suggesting that the electronic configuration and site symmetry of Ca atoms in these CDHA crystals are not significantly different. A similar observation for Ca/P values of 1.55, 1.59 and 1.68 was also reported by Sugiyama et al., but no detailed interpretation in the XANES spectra was clarified in their studied [26–28].

There are two ways to interpret XANES spectra. One is the fingerprint method in which the XANES of the material of interest is compared with the XANES of other materials of known structures to identify structural similarities. The other method is to compare the XANES of the materials of interest with the results of molecular orbital density of state calculations since the XANES spectrum is a reflection on the empty states above the Fermi energy. Therefore, the fingerprint method has been used in this study to interpret the
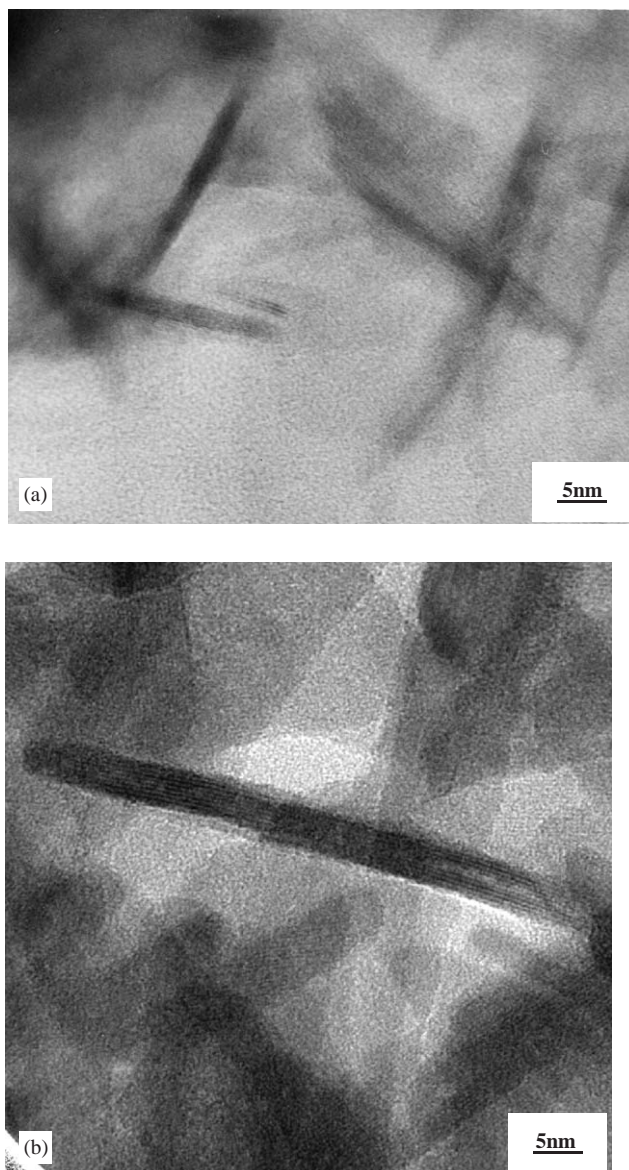
Fig. 4. High-resolution TEM image of the needle-like CDHA nano-crystals with (a) Ca/P = 1.5 and (b) Ca/P = 1.67.

Fig. 5. (a) FT of Ca K-edge EXAFS for CDHA nano-crystals with different Ca/P ratios and (b) the magnified area around the peak of 0.25 nm.

XANES spectra of these CDHA crystals with Ca/P ratios of 1.5, 1.55, 1.6 and 1.67.

The weak pre-peak A in Fig. 6(a) before the rising absorption edge may be attributed to the 1s→3d transition, being dipole forbidden ($\Delta \ell = 2$), resulting from mixing of unoccupied d final states with p-character final states. The shoulder peak B on the rapidly rising absorption curve is assigned to the 1s→4s transition and the principal peak C is assigned to the allowed 1s→4p transition. The area around peak C is magnified and illustrated in Fig. 6(b). It was observed that the Ca K-edge of HA has a higher absorption coefficient than that of other CDHA nano-crystals with a Ca/P ratio less than 1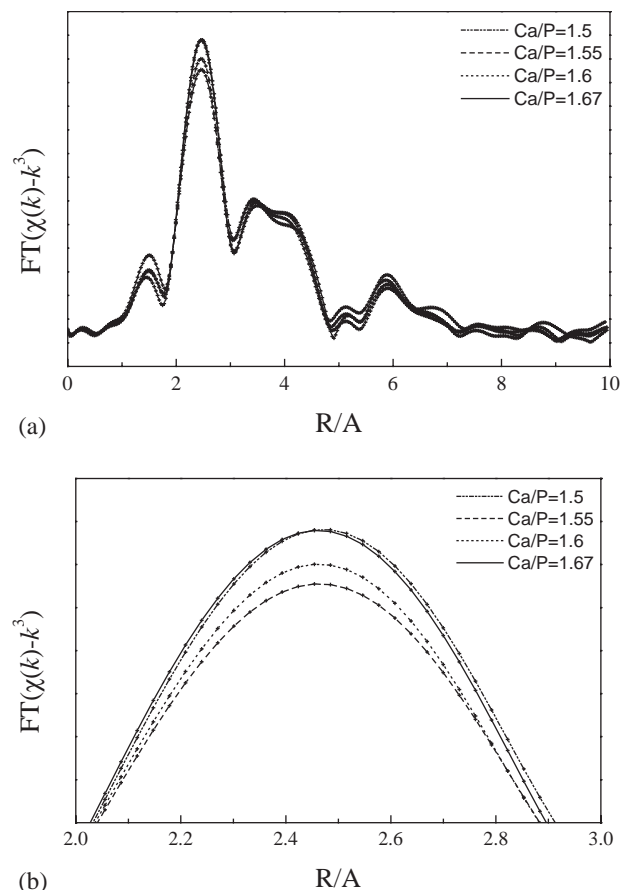.67. If the fluorescence mode is a predominant factor, the absorption coefficient is dependent on the concentration of absorbing atom and higher concentration of the absorbing atom corresponds to higher absorption coefficient. Although the concentration of Ca atom per volume follows 1.67 > 1.6 > 1.55 > 1.5, the order of absorption coefficient is found to be 1.67 > 1.5 > 1.6 > 1.55 in our results. It seems to imply that the fluorescence mode is not a predominant factor affecting the absorption coefficient. As discussed above, the concept of stoichiometry and non-stoichiometry is more appropriate for elucidating the difference of absorption coefficient in the CDHA nano-crystals with different Ca/P values.

3.4. Electron energy loss analysis

It has been demonstrated that the EELS is a powerful instrument for analyzing the structural and chemical environment of the nano-scaled region such as nano-sized crystals or powders [29]. Therefore, this technique was performed for all the CDHA nano-crystals with Ca/P ratios from 1.5 to 1.67. Owing to the problem related to the monochromating incident beam, the XAS studies
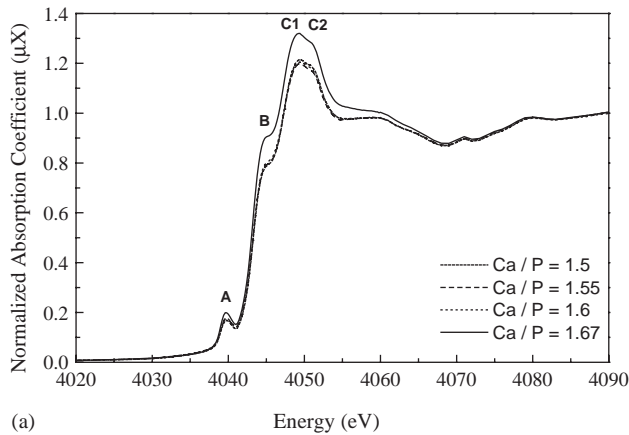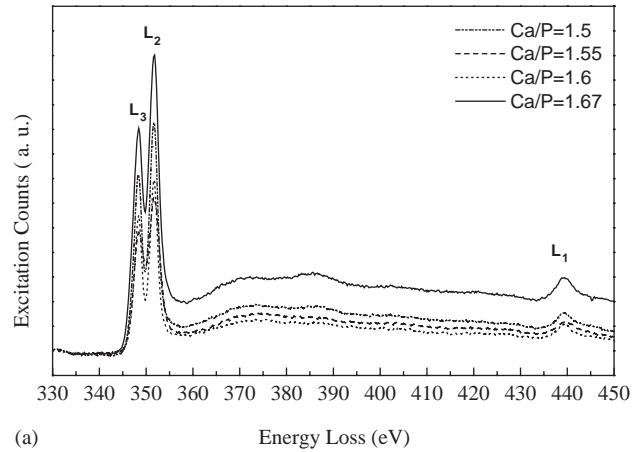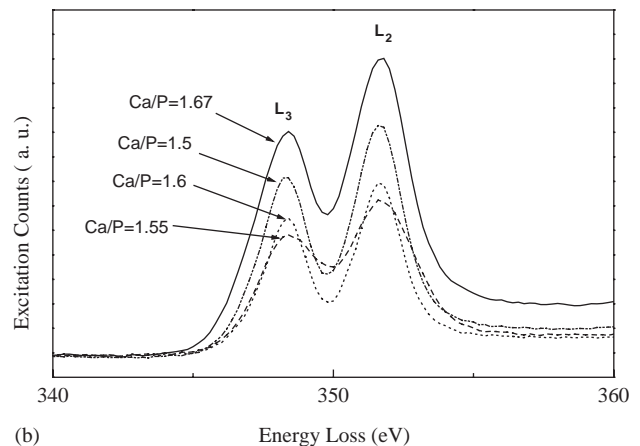
(a)
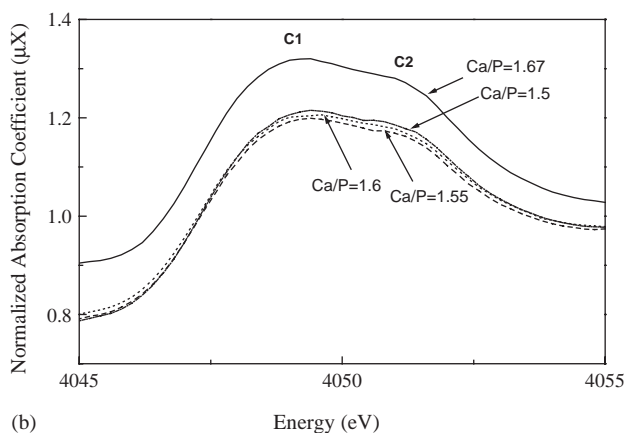
(b)

Fig. 6. (a) XANES spectra near the Ca K-edge of calcium-deficient apatites with different Ca/P ratios and (b) the magnified area around peak C.

(a)

(b)

Fig. 7. (a) ELNES spectra near the Ca $L_{2,3}$-edge of calcium-deficient apatites with different Ca/P ratios and (b) the magnified energy-loss range from 340 to 360 eV.

have concentrated on the calcium K-edge. On the other hand, EELS is ideally suitable for measuring energy loss below 2 keV and allows to perform the calcium L-edges. After background substitution, the electron-energy loss near-edge structure (ELNES) of Ca $L_{2,3}$-edge and L_1-edge for all the CDHA crystals are seen in the energy-loss region, as illustrated in Fig. 7(a). The shape of Ca $L_{2,3}$-edge displays two split sharp lines (called white-lines) since they were first observed in X-ray absorption spectra on a photographic plate [30]. Following the dipole selection rule, the L_3 and L_2 edge spectra correspond to transitions of $2p^{3/2} \rightarrow 3d^{3/2}3d^{5/2}$ and $2p^{1/2} \rightarrow 3d^{3/2}$, respectively [31–35]. The L_1-edge appearing in the EELS spectrum indicates that the 4p orbitals are not filled in the CDHA crystals. It was observed that the ELNES for all the CDHA nano-crystals with Ca/P values of 1.5, 1.55, 1.6 and 1.67 presents a similar feature as shown in Fig. 7(a). It seems to imply that the coordination of Ca atoms has the same charge state and site symmetry.

The excitation counts of $L_{2,3}$-edges with energy-loss ranging from 340 to 360 eV can be magnified and

shown in Fig. 7(b), revealing that the magnitude of excitation count is 1.67 > 1.5 > 1.6 > 1.55. Furthermore, the excitation count of Ca $L_{2,3}$-edge in the ELNES exhibits the same trend like XANES of the Ca K-edge. Consequently, the previous discussion of stoichiometry and non-stoichiometry from XANES plays a more important role in explaining the difference in excitation counts of the CDHA crystals with different Ca/P ratios. Therefore, the excitation counts of stoichiometric HA and apatite-TCP is higher than that of non-stoichiometric apatites. When the structure disorder was also considered, the excitation count of the stoichiometric HA (Ca/P = 1.67) is larger than that of apatite-TCP (Ca/P = 1.5) but for the non-stoichiometric apatites, the CDHA with 1.6 shows a higher excitation count than that with 1.55.

Based on the above discussion, it is found that different chemical and biological properties between CDHA and HA can be further distinguished and clarified by structure analysis with EXAFS, XANES and EELS even though their XRD patterns appear undistinguished.

4. Conclusion

The synthesis of single-phased needle-like CDHA nano-crystals with Ca/P ratios from 1.5 to 1.67 can be performed by a simple coprecipitation method with a good reproducibility. The amplitude of FT in the EXAFS spectra indicates that the structural disorder increases following the sequence of $1.67 > 1.5 > 1.6 > 1.55$, implying that stoichiometry and non-stoichiometry plays a more important role than the structural order–disorder. This may suggest that different biochemical properties between Ca/P $= 1.5$ and 1.67 is mostly due to the effect of stoichiometry and non-stoichiometry.

Acknowledgements

References

[1] Liu DM, Troczynski T, Tseng WJ. Water-based sol–gel synthesis of hydroxyapatite: process development. Biomaterials 2001;22:1721–30.

[2] Ginebra MP, Fernandez E, Driessens FCM, Planell FA. Modeling of the hydrolysis of α-tricalcium phosphate. J Am Ceram Soc 1999;82(10):2808–12.

[3] Elliott J. Structure and chemistry of the apatites and other calcium orthophosphates. New York: Elsevier; 1994.

[4] Bett JAS, Christner LG, Hall WK. Studies of the hydrogen held by solids. XII. Hydroxyapatite catalysts. J Am Chem Soc 1967;89(22):5535–41.

[5] Honma H. Catalytic behavior of calcium phosphate for decompositions of 2-propanol and ethanol. J Catal 1982;75:200–3.

[6] Sugiyama S, Minami T, Moriga T, Hayashi H, Koto K, Tanaka M, Moffat JB. Surface and bulk properties, catalytic activities and selectivities in methane oxidation on near-stoichiometric calcium hydroxyapatites. J Mater Chem 1996;6(3):459–64.

[7] Sugiyama S, Minami T, Moriga T, Hayashi H, Tanaka M, Shigemoto N, Moffat JB. Enhancement of the selectivity to carbon monoxide with feedstream doping by tetrachloromethane in the oxidation of methane on stoichiometric calcium hydroxyapatite. J Chem Soc Faraday Trans 1996;92(2):293–9.

[8] Suzuki T, Hatsushika T, Miyake M. Synthetic hydroxyapatites as inorganic cation exchangers. J Chem Soc Faraday Trans 1 1982;78:3605–11.

[9] Sugiyama S, Minami T, Goda M, Hayashi H, Moffat JB. Effects of fine structure changes of strontium hydroxyapatites on ion-exchange properties with divalent cations. J Chem Soc Faraday Trans 1996;92(21):4305–10.

[10] Meyer JL, Fowler BO. Lattice defects in nonstoichiometric calcium hydroxyapatites. A chemical Approach. Inorg Chem 1982;21:3029–35.

[11] Mortier A, Lemaitre J, Rodrique L, Rouxhet PG. Synthesis and thermal behavior of well-crystallized calcium-deficient phosphate apatite. J Solid State Chem 1989;78:215–9.

[12] Narasaraju TSB, Phebe DE. Review some physico-chemical aspects of hydroxylapatite. J Mater Sci 1996;31:1–21.

[13] Vallet-Regi M, Rodriguez-Lorenzo LM, Salinas AJ. Synthesis and characterization of calcium deficient apatite. Solid State Ionic 1997;101–103:1279–85.

[14] Ishikawa K, Ducheyne P, Radin S. Determination of the Ca/P ratio in calcium-deficient hydroxyapatite using X-ray diffraction analysis. J Mater Sci: Mater Med 1993;4:165–8.

[15] Raynaud S, Champion E, Bernache-Assollant D, Thoman P. Calcium phosphate apatites with variable Ca/P atomic ratio I. Synthesis, characterization and thermal stability of powders. Biomaterials 2002;23:1065–72.

[16] Liou SZ, Chen SY. Transformation mechanism of different chemically precipitated apatitic precursors into β-tricalcium phosphate upon calcinations. Biomaterials 2002;23:4541–7.

[17] Layani JD, Cuisinier FJG, Steuer P, Cohen H, Voegel JC, Mayer I. High-resolution electron microscopy study of synthetic carbonate and aluminum containing apatites. J Biomed Mater Res 2000;50:199–207.

[18] Suvorova EI, Buffat PA. Electron diffraction from micro- and nanoparticles of hydroxyapatite. J Microsc 1999;196:46–58.

[19] Nicolopoulos S, Gonza'lez-Calbet JM, Alonso MP, Gutierrez-Rios MT, de Frutos MI, Vallet-Regi M. Characterization by TEM of local crystalline changes during irradiation damage of hydroxyapatite compounds. J Solid State Chem 1995;116: 265–74.

[20] Nelson DGA, Wood GJ, Barry JC, Featherstone JDB. The structure of (100) defects in carbonated apatite crystallites: a high resolution electron microscope study. Ultramicroscopy 1986;19:253–66.

[21] Durham PJ. Theory of XANES. X-ray absorption: principles, applications, techniques of EXAFS, SEXAFS, and XANES. New York: Wiley; 1988 (Chapter 2).

[22] Harries JE, Hukins DWL, Hasnain SS. Analysis of the EXAFS spectrum of hydroxyapatite. J Phys C: Solid State Phys 1986;19:6859–72.

[23] Smart L, Moore E. Solid state chemistry. London: Chapman & Hall; 1992. p. 125–6.

[24] West AR. Basic solid state chemistry. New York: Wiley; 1999. p. 126.

[25] Lacout JL. Calcium phosphates as bioceramics. In: Muster D, editor. Biomaterials—hard tissue repair and replacement. Amsterdam: Elsevier Science; 1992. p. 81.

[26] Sugiyama S, Moriga T, Goda M, Hayashi H, Moffat JB. Effect of fine structure changes of strontium hydroxyapatites on ion-exchange properties with divalent cations. J Chem Soc Faraday Trans 1996;92(21):4305–10.

[27] Sugiyama S, Minami T, Moriga T, Hayashi H, Koto K, Tanaka M, Moffat JB. Surface and bulk properties, catalytic activities and selectivities in methane oxidation on near-stoichiometric calcium hydroxyapatites. J Mater Chem 1996;6(3):459–64.

[28] Sugiyama S, Yasutomi T, Moriga T, Hayashi H, Moffat JB. Preparative enhancement of the thermal stability of calcium hydroxyapatites. J Solid State Chem 1999;142:319–24.

[29] Egerton RF. Electron energy-loss spectroscopy in the electron microscope. New York: Plenum Press; 1996.

[30] Williams DB, Carter CB. Transmission electron microscopy: a textbook for materials science. New York: Plenum Press; 1996. p. 691.

[31] Leapman RD, Grunes LA, Fejes PL. Study of the L_{23} edges in the 3d transition metals and their oxides by the electron-energy-loss spectroscopy with comparisons to theory. Phys Rev B 1982; 26(1):614–35.

[32] Waddingto WG, Rez P, Grant IP, Humphreys CJ. White lines in the $L_{2,3}$ electron-energy-loss and X-ray absorption spectra of 3d transition metals. Phys Rev B 1986;34(3):1467–73.

[33] de Groot FMF, Fuggle JC, Thole BT, Sawatzky GA. $L_{2,3}$ X-ray-absorption edges of d^0 compounds: K^+, Ca^{2+}, Sc^{3+}, and Ti^{4+} in O_h (octahedral) symmetry. Phys Rev B 1990;41(2):928–37.

[34] Pearson DH, Ahn CC, Fultz B. White lines and d-electron occupancies for the 3d and 4d transition metals. Phys Rev B 1993;47(14):8471–8.

[35] Manson ST. The calculation of photoionization cross sections: an atomic view. Topics in Applied Physics, vol. 26. New York: Springer; 1978. p. 135–63.